Demonstration of Single-Shot Picosecond Time-Resolved MeV Electron Imaging Using a Compact Permanent Magnet Quadrupole Based Lens

D. Cesar, J. Maxson, P. Musumeci, and Y. Sun
Department of Physics and Astronomy, UCLA, Los Angeles, California 90095, USA

J. Harrison
Department of Electrical Engineering, UCLA, Los Angeles, California 90095, USA

P. Frigola, F. H. O'Shea, and H. To
RadiaBeam Technologies, 1717 Stewart Street, Santa Monica, California 90404, USA

D. Alesini
INFN-LNF, Via E. Fermi, 40-00044 Frascati, Rome, Italy

R. K. Li
SLAC National Accelerator Laboratory, Menlo Park, California 94025, USA
(Received 12 April 2016; published 7 July 2016)

We present the results of an experiment where a short focal length (~1.3 cm), permanent magnet electron lens is used to image micron-size features (of a metal sample) with a single shot from an ultrahigh brightness picosecond-long 4 MeV electron beam emitted by a radio-frequency photoinjector. Magnification ratios in excess of 30× were obtained using a triplet of compact, small gap (3.5 mm), Halbach-style permanent magnet quadrupoles with nearly 600 T/m field gradients. These results pave the way towards single-shot time-resolved electron microscopy and open new opportunities in the applications of high brightness electron beams.

DOI: 10.1103/PhysRevLett.117.024801

Transmission electron microscopy (TEM) is one of the primary tools for materials characterization, with many scientific and industrial applications. One of the recent trends in TEM development is the quest for *in situ* dynamic imaging in which a sequence of micrographs are captured in a time-resolved mode while the sample under study is undergoing some sort of microscopic rearrangement [1–3].

Improving the temporal resolution of TEMs to ultrafast time scales introduces significant challenges. In order to substantially decrease the image acquisition time, it is necessary to increase the peak current by many orders of magnitude. But at large currents the temporal resolution and transverse coherence rapidly degrade due to Coulomb interactions between the beam electrons [4]. Thus, state-of-the-art single-shot TEM systems have been limited to 10 nm, 10 ns spatiotemporal resolution [5,6]. The only known remedy has been to reduce the number of charged particles per pulse and integrate over many millions of shots in order to collect a single picture [7]. This technique has produced a variety of scientific results [8], but it is restricted to fully reversible processes.

Single-shot picosecond transmission electron microscopy (SPTEM) would fill an unmet need in the TEM community to image irreversible dynamical motion at nanometer-picosecond spatiotemporal scales, enabling real time study of the dynamics of many technologically and scientifically relevant microscopic processes, such as phase transitions and dislocation motion [9,10]. One path to SPTEM requires replacing the 100 keV typical of conventional TEMs with MeV electrons in order to take advantage of the relativistic suppression of the space-charge effects. This solution, discussed in detail in [11], involves a redesign of the microscope architecture based on the highest peak brightness source of relativistic electrons available to date, the radio-frequency (rf) photoinjector.

rf photoguns have played a central role in the development of the high brightness beams used in x-ray free-electron lasers [12]. By combining the high current densities available in photoemission with the extremely high fields of a standing wave rf cavity, the rf photoinjector has already demonstrated the capability of generating MeV electron beams bright enough to capture single-shot diffraction patterns with a shutter speed of less than 100 fs [13–16].

One of the main challenges for SPTEM comes from the fact that the high electron energy, which conveniently limits the influence of Coulomb self-fields, comes at the cost of increased magnetic rigidity. High voltage (1–3 MeV) electron microscopes were, until the advent of aberration correction, one of the main candidates for improving the spatial resolution in TEM to the atomic level [17]. These machines were overburdened by large and expensive magnetic lenses weighing up to several tons. The

unfavorable scaling of focusing power in a round magnetic lens ("solenoid") as the inverse square of the electron energy poses a practical limit to the development of time-resolved electron microscopy [18,19] and calls for the introduction of very strong magnetic lenses and/or of novel focusing elements.

Our approach borrows from experience in the field of advanced accelerators and involves the use of permanent magnet quadrupole (PMQ) lenses for imaging with relativistic electrons. PMQ triplets provide a compact short-focal-length lens for use by inverse Compton scattering sources [20] and advanced accelerator applications [21].

In this Letter, we report on using a picosecond-long 4 MeV electron beam from an rf photoinjector and a strong compact PMQ-based lens with a focal length of ~1.3 cm to obtain single-shot micrographs with micron-scale spatial resolution. The quadrupoles used in our experiment were measured to have field gradients of nearly 600 T/m, which, to our knowledge, set a new record for the strongest quadrupoles ever built. Magnification factors larger than 30× have been achieved. These results represent the first example of single-shot picosecond time-resolved transmission electron microscopy.

The experiment was performed at the UCLA Pegasus Laboratory [22], where a 1.6 cell *S*-band rf gun, fabricated using a brazeless clamped design [23] is used to generate a high brightness electron beam. In order to maximize image sharpness, the photoinjector is operated in an ultralow emittance configuration in which the laser spot on the cathode is minimized (8×12 μm). This is achieved by illuminating the photocathode from a 72° port located in the first cell of the rf cavity, which allows the use of a high power final focus lens ($f = 17.5$ cm). The small source size enables minimization of the initial phase space area, which is preserved during transport because the beam rapidly expands transversely into a uniformly filled ellipsoid [24].

The beam is transported to the microscope sample plane located 3.7 m from the cathode using two round electromagnetic lenses ("gun solenoids," $f \gtrsim 0.5$ m) which provide flexibility [25] in choosing sample illumination. In principle, PMQ-based lenses could be used in the condenser stage, but simulations showed that the existing solenoids were sufficient for illuminating the sample with micron-size beams. The transverse beam parameters are characterized by inserting a thin (20 μm) YAG screen located shortly before the sample plane. The screen is imaged by an in-vacuum optical microscope objective with a 1 μm spatial resolution limited by a narrow depth of focus. On this screen, the rms spot can be made as small as 3 μm, with a normalized emittance (measured by scanning the solenoid current) of 5 nm, for a 20 fC beam. For larger beam charges (up to 100 fC), as employed in the experiments, the normalized emittance is measured below 20 nm in agreement with simulations performed using the general particle tracer (GPT) code [26]. The electron beam duration was measured to be 0.9 ± 0.15 ps (rms) using an *x*-band deflecting cavity operated as a streak camera located shortly after the microscope [27].

Shortly after the sample sits a set of PMQs designed to form an image of the sample 41 cm downstream. The simplest (fewest elements) lens design to achieve imaging with equal magnification in both transverse dimensions requires three PMQs arranged analogous to those in Table I. Solutions with four or more quadruples, such as the antisymmetric ("Russian") quadruplet, are very attractive, because they can provide equal magnification in all configurations and they can reduce aberrations [28]; however, such designs require tighter manufacturing tolerances and therefore were not considered for this proof-of-principle experiment.

Each PMQ is made up of grade N35SH NbFeB wedges wire electrical discharge machined and assembled into a 16 sector Halbach-style array [29] with an inner diameter of 3.5 mm and an outer diameter of 7 mm (see Fig. 2 for the wedge magnetization orientation and resulting field profile). The triplet is housed in a custom flexure stage allowing the user to adjust the longitudinal position of each magnet and obtain imaging for input beam energies between 3.5 and 4.75 MeV. The total weight of the lens is less than 2 pounds.

A vibrating wire technique was used to prealign the magnetic axis and measure the integrated field gradients [30]. The integrated gradient matches the field profile calculated using the electrostatic solver Radia [31]. Radia is used to determine the peak field gradient and effective magnet length listed in Table I.

Radia is also used to generate field maps used to simulate beam dynamics in the microscope. These field maps permit detailed simulations of the microscope column beam dynamics. We begin by solving a linear transport model of hard-edge quadrupoles to find out the beam line distances required to achieve an imaging condition with equal magnifications in x and y at the detector plane. We then refine the calculation by using the quadrupole gradient

TABLE I. Parameters for the PMQ triplet. The reference position is measured from the sample plane.

	Design gradient	Effective length	Measured $G \times L$	Reference design position
First quadrupole	597 T/m	6.16 mm	3.3 ± 0.4 T	5.25 mm
Second quadrupole	−597 T/m	6.16 mm	3.6 ± 0.5 T	11.25 mm
Third quadrupole	495 T/m	3.6 mm	1.7 ± 0.2 T	17.25 mm

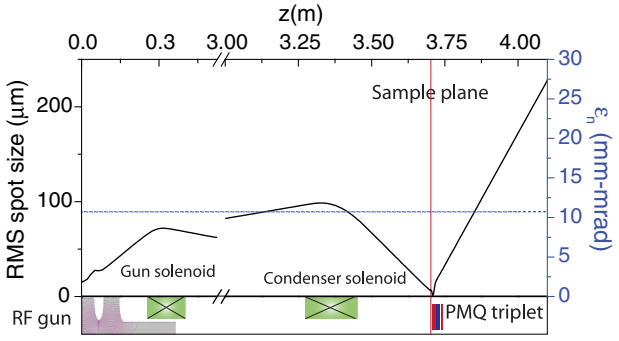

FIG. 1. Schematic of the MeV TEM Pegasus beam line. Note that solenoid refers here to a round electromagnetic lens with an iron yoke and pole pieces. The evolution of the rms spot size and normalized emittance ϵ_n along the beam line from a GPT simulation for a 50 fC beam charge are also reported. Note the axis break.

profile along the beam line axis, z. Finally, tracking the particle trajectories in the full PMQ triplet magnetic field maps was used to estimate the transverse tolerance to misalignment and the aberrations of the system. The results are shown in Fig. 3. The calculated spherical aberrations for the manufactured PMQs are 8.9 and 75.2 mm in the horizontal (focusing first) and vertical (defocusing first) principal planes, respectively. It was also found that for each quadrupole an angular misalignment of ± 10 μrad and a transverse displacement of 50 μm with respect to the central beam trajectory were required in order to avoid degradation of the image quality.

A 20 ± 5 μm thick Cu "UCLA" sample target was fabricated using lithographic techniques with varied feature sizes from 5 to 100 μm. The target was mounted on a 3 mm standard TEM holder and inserted in the beam line using a

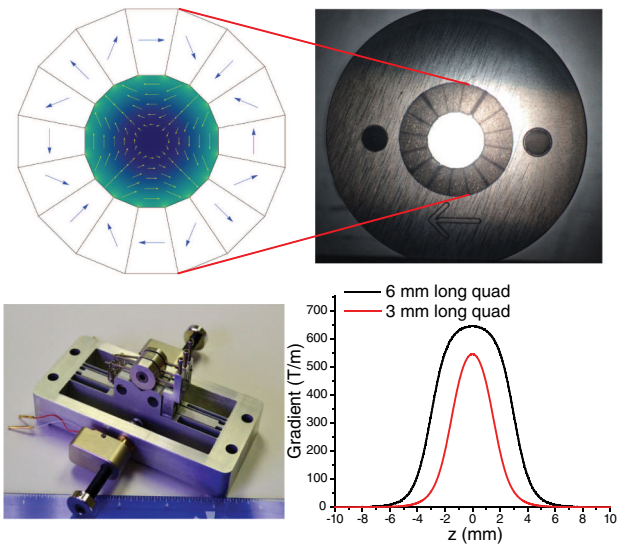

FIG. 2. (a) 3d magnetic field map for an ideal Halbach PMQ. (b) Photo of a single PMQ. (c) Picture of the PMQ triplet setup. (d) Magnetic field profile of the PMQs from 3D Radia simulations.

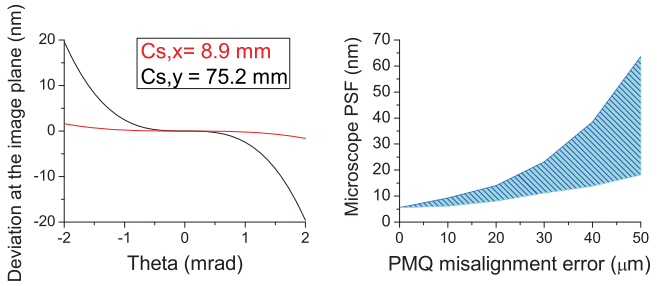

FIG. 3. (a) Aberrations for the PMQ triplet. (b) Tolerances to misalignment of the three-element lens. The shaded area is obtained by calculating the rms size of the beam at the detector plane after tracking a very small source of electrons with 1 mrad divergence when each quadrupole is displaced in a random direction in the transverse plane by a fixed amount.

micrometer translation stage 500 μm from the front face of the first PMQ. Because the imaging condition is achieved by translating the individual quadrupoles, extra care must be taken when installing the triplet stage. For this reason, a HeNe laser copropagating with the electron beam is used to align the sample and the triplet stage to the electron beam line axis. The image was collected using a 100 μm thick YAG screen lens-coupled to a Princeton Instrument PIMAX III intensified camera. The point spread function (psf) of this phosphor screen-based imaging system (not to be confused with the psf of the microscope itself, which depends on the magnification) is estimated to be 50 μm rms, mostly attributable to the screen thickness.

An optical image of the sample is shown next to a representative single-shot electron image of the sample in Figs. 4(a) and 4(b). All of the sample features are clearly visible in the electron image, as is a contaminant which was introduced above the "U" during sample preparation. The skewness of the electron image is accentuated by alignment error: The sample does not sit precisely perpendicular to or centered on the PMQ axis. The dimensions of the letters in the electron image can be used to compute a magnification

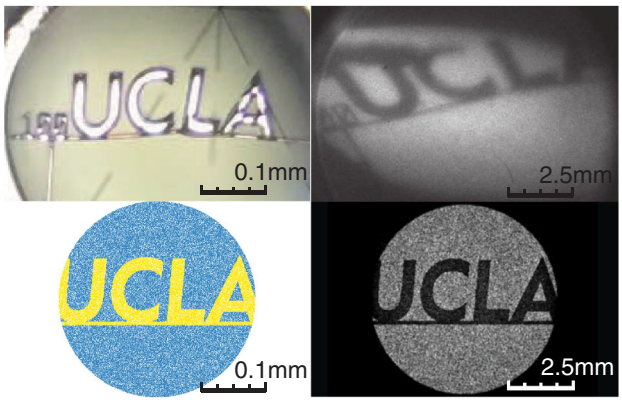

FIG. 4. (a) Optical and (b) electron image of the nanofabricated UCLA target. (c) Simulated distribution at the target. The color coding indicates division between scattered and unscattered particles. (d) Simulated distribution at the image plane.

of 32× and 25× in the horizontal and vertical plane, respectively, in fair agreement with the design magnification of 25× [Figs. 4(c) and 4(d)]. The astigmatism is caused by a small amount of defocus and could be removed by fine-tuning the quadrupole positions.

A quantitative comparison of the simulated and recorded electron images requires a complete understanding of the electron imaging apparatus. Start-to-end simulations of the image formation process are performed, taking into account multiple elastic and inelastic scattering of electrons inside the sample. This is included in the particle tracking simulations by assigning an additional divergence and energy spread for particles that hit the metallic sample, accounting for the multiple elastic scattering and inelastic collisions, respectively [32,33]. The full simulation (Fig. 4) shows that contrast is created when scattered electrons are clipped by the aperture of the magnets. Additional contrast is provided by the imperfect imaging of the lower energy electrons.

In both the simulation and experiment, the highest resolution electron images are obtained at the maximum sample illumination flux, $n_e = 18$ electrons/μm^2. Li and Musumeci [11] showed that, as the charge density is increased beyond a certain optimum level, space charge effects and point-to-point scattering will cause image blurring. Given the relatively small magnification factor and large feature sizes, the impact of Coulomb scattering could not be measured in this experiment. Nevertheless, by varying the condenser lens strength, we were able to quantify the effect of changes in the illumination flux on the image sharpness.

In Fig. 5, we show the resolution in both experimental and simulated images quantified as the standard deviation of the centroid positions of error-function fits to the lineouts taken along the edge of the "L" in the UCLA sample. The data points are obtained from a series of images captured with different condenser excitation currents and beam charges (to vary n_e). GPT simulations are then performed using the measured illumination fluences. Both the data and simulation show that the noise (and therefore the image sharpness) improves as the fluence is increased. Assuming Poisson statistics for the signal, we expect the spatial resolution in the image to scale as $1/n_e$ according to the Rose criterion [34]. The inherent psf of the detector system further limits the spatial resolution. In order to quantify this, a Gaussian blur of 20 μm (at the detector plane, and therefore 0.7 μm at the sample plane considering the 30× magnification) was taken into account when computing the simulated images. The main difference between the experimental and simulated curves is their asymptotic high-fluence limit, which can be traced back to the differences between the simulated and real point spread functions discussed above. Figure 5 serves to show that the resolution of the current microscope setup could be further enhanced by improving the detection system [35].

For small image features, the resolution becomes intertwined with contrast such that understanding and improving contrast is a necessary component of a high magnification system. Contrast is defined from the image intensity as $(I_{\max} - I_{\min})/(I_{\max} + I_{\min})$. In Fig. 6, we show four simulated curves demonstrating the effect that adding an objective aperture would have on the image contrast. The two solid lines show the simulated contrast for copper and gold versions of the UCLA target. The effect of the iris size is more dramatic for the copper target, since copper scatters the electrons less than gold. The rms angular and energy spread of the Gaussian distributions of the particles hitting the samples are $\theta_{\mathrm{Cu}} = 0.1$, $\Delta E_{\mathrm{Cu}} = 29$ keV and $\theta_{\mathrm{Au}} = 0.2$, $\Delta E_{\mathrm{Au}} = 68$ keV for copper and gold, respectively. The contrast of a copper target for an aperture equal to the gap between the PMQ magnets (3.5 mm) is 0.43, in close agreement with the 0.42 contrast obtained from analysis of the line profiles of the L in the electron images.

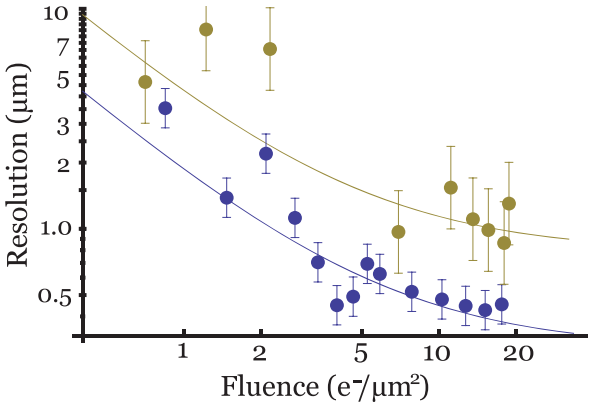

FIG. 5. Microscope resolution as a function of charge for simulated (blue) and measured (gold) data. The error bars on the simulations are due to the random particle initialization. The solid lines show the $1/n_e$ scaling for the resolution.

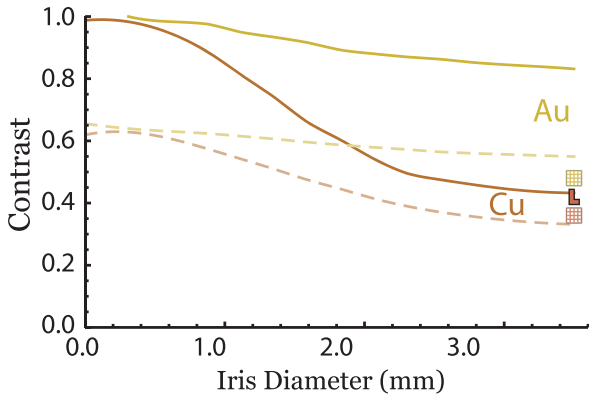

FIG. 6. Simulated contrast as a function of the objective iris aperture for copper and gold targets having feature sizes similar (dashed line) or well under (solid line) the spatial resolution of the microscope. Also shown are the contrast of the three samples (UCLA target and Cu and Au TEM grids) observed experimentally using the PMQ gap as an iris aperture.

Also shown are two dashed lines showing the results of simulations of image formation for objects having sizes similar to the psf of the detection system. In such cases, the differences between gold and copper samples are significantly smaller, as the contrast is dominated by the resolution not by the sample scattering properties. These simulations can be compared to the measured contrast from 5 μm bars on gold and copper TEM 2000 grids, shown in Fig. 6 above and below the L, respectively. Future single-shot time-resolved TEMs will require using an iris to increase the percentage of scattered electrons which are clipped. Diffraction contrast could also be obtained by positioning slits at the back focal plane(s) of the lens.

In conclusion, these experiments demonstrate the first single-shot, picosecond time-resolved electron images. They were created using high brightness, relativistic electrons from an rf photoinjector and were imaged by novel, record-high gradient PMQ-based objective lens. Further work is required in order to stage multiple PMQ lenses to increase the magnification and reach the resolution limit, which, in single-shot electron microscopy, is ultimately set by space-charge-induced blurring [11]. The compact lens design discussed in this Letter offers a significant reduction in size, cost, and focal length for electrons at MeV energies —for which Coulomb interactions are suppressed by relativistic effects. Furthermore, quadrupole-based lenses might also offer an additional advantage over round lenses due to the smaller charge density that is obtained in elliptical crossovers. The results reported in this Letter validate the simulation models of the beam dynamics in the relativistic electron column and image formation process, paving the way towards the use of bright relativistic electron sources to achieve the long-range goal for single-shot time-resolved TEM of being able to follow defect dynamics in materials with 10 nm spatial resolution and picosecond temporal resolution.

This work was partially supported by DOE STTR Grant No. DE-SC0013115 and National Science Foundation Grant No. PHY-1415583. The authors acknowledge A. Murokh and G. Andonian for useful discussions.

[1] W. E. King, G. H. Campbell, A. Frank, B. Reed, J. F. Schmerge, B. J. Siwick, B. C. Stuart, and P. M. Weber, Ultrafast electron microscopy in materials science, biology, and chemistry, J. Appl. Phys. **97**, 111101 (2005).

[2] A. H. Zewail, Four-dimensional electron microscopy, Science **328**, 187 (2010).

[3] science.energy.gov/bes/community-resources/reports/abstracts/#EXD.

[4] B. W. Reed, M. R. Armstrong, N. D. Browning, G. H. Campbell, J. E. Evans, T. LaGrange, and D. J. Masiel, The evolution of ultrafast electron microscope instrumentation, Microsc. Microanal. **15**, 272 (2009).

[5] T. B. LaGrange *et al.*, Single-shot dynamic transmission electron microscopy, Appl. Phys. Lett. **89**, 044105 (2006).

[6] N. Browning *et al.*, Recent developments in dynamic transmission electron microscopy, Curr. Opin. Solid State Mater. Sci. **16**, 23 (2012).

[7] B. Barwick, H. S. Park, O. H. Kwon, J. S. Baskin, and A. H. Zewail, 4D imaging of transient structures and morphologies in ultrafast electron microscopy, Science **322**, 1227 (2008).

[8] B. Barwick, D. Flannigan, and A. H. Zewail, Photon-induced near-field electron microscopy, Nature (London) **462**, 902 (2009).

[9] T. Lagrange, B. W. Reed, W. E. King, J. S. Kim, and G. H. Campbell, in *In-Situ Electron Microscopy: Applications in Physics, Chemistry and Materials Science*, edited by G. Dehm, J. M. Howe, and J. Zweck (Wiley-VCH, Weinheim, 2012).

[10] F. Carbone, P. Musumeci, O. J. Luiten, and C. Hebert, A perspective on novel sources of ultrashort electron and X-ray pulses, Chem. Phys. **392**, 1 (2012).

[11] R. K. Li and P. Musumeci, Single-Shot MeV Transmission Electron Microscopy with Picosecond Temporal Resolution, Phys. Rev. Applied **2**, 024003 (2014).

[12] P. Emma *et al.*, First lasing and operation of an ångstrom-wavelength free-electron laser, Nat. Photonics **4**, 641 (2010).

[13] P. Musumeci, J. T. Moody, C. M. Scoby, M. S. Gutierrez, and M. Westfall, Laser-induced melting of a single crystal gold sample by time-resolved ultrafast relativistic electron diffraction, Appl. Phys. Lett. **97**, 063502 (2010).

[14] S. P. Weathersby *et al.*, Mega-electron-volt ultrafast electron diffraction at SLAC National Accelerator Laboratory, Rev. Sci. Instrum. **86**, 073702 (2015).

[15] Y. Muro'oka, N. Naruse, S. Sakakihara, M. Ishimaru, J. Yang, and K. Tanimura, Transmission-electron diffraction by MeV electron pulses, Appl. Phys. Lett. **98**, 251903 (2011).

[16] S. Manz *et al.*, Mapping atomic motions with ultrabright electrons: towards fundamental limits in space-time resolution, Faraday Discuss. **177**, 467 (2015).

[17] J. C. H. Spence, *High Resolution Electron Microscopy* (Oxford University, New York, 2003).

[18] D. Xiang, F. Fu, J. Zhang, X. Huang, L. Wang, X. Wang, and W. Wan, Accelerator-based single-shot ultrafast transmission electron microscope with picosecond temporal resolution and nanometer spatial resolution, Nucl. Instrum. Methods Phys. Res., Sect. B **759**, 74 (2014).

[19] J. Yang, in Proceedings of the Workshop on Ultrafast Electron Sources for Diffraction and Microscopy, Los Angeles, CA, 2012 (unpublished).

[20] J. K. Lim, P. Frigola, G. Travish, J. B. Rosenzweig, S. G. Anderson, W. J. Brown, J. S. Jacob, C. L. Robbins, and A. M. Tremaine, Adjustable, short focal length permanent-magnet quadrupole based electron beam final focus system, Phys. Rev. ST Accel. Beams **8**, 072401 (2005).

[21] C. M. S. Sears, R. L. Byer, E. R. Colby, B. M. Cowan, R. Ischebeck, M. R. Lincoln, T. Plettner, R. H. Siemann, and J. E. Spencer, Beam coupling to optical scale acceleration structures, AIP Conf. Proc. **877**, 665 (2006).

[22] P. Musumeci, J. T. Moody, R. J. England, J. B. Rosenzweig, and T. Tran, Experimental Generation and Characterization

of Uniformly Filled Ellipsoidal Electron-Beam Distributions, Phys. Rev. Lett. **100**, 244801 (2008).
[23] D. Alesini *et al.*, New technology based on clamping for high gradient radio frequency photogun, Phys. Rev. ST Accel. Beams **18**, 092001 (2015).
[24] R. K. Li, K. G. Roberts, C. M. Scoby, H. To, and P. Musumeci, Nanometer emittance ultralow charge beams from rf photoinjectors, Phys. Rev. ST Accel. Beams **15**, 090702 (2012).
[25] B. W. Reed, T. LaGrange, R. M. Shuttlesworth, D. J. Gibson, G. H. Campbell, and N. D. Browning, Solving the accelerator-condenser coupling problem in a nanosecond dynamic transmission electron microscope, Rev. Sci. Instrum. **81**, 053706 (2010).
[26] http://www.pulsar.nl/gpt/.
[27] R. J. England *et al.*, X-Band Dipole Mode Deflecting Cavity for the UCLA Neptune Beamline, in *Proceedings of the 2005 Particle Accelerator Conference* (IEEE, New York, 2005), pp. 2627–2629.
[28] P. W. Hawkes, *Quadrupoles in Electron Lens Design*, Vol. 7 (Academic, New York, 1970).
[29] K. Halbach, Design of permanent multipole magnets with oriented rare earth cobalt materia, Nucl. Instrum. Methods **169**, 1 (1980).
[30] Z. Wolf, SLAC Report No. LCLS-TN-05-11, 2005, http://www-ssrl.slac.stanford.edu/lcls/technotes/LCLS-TN-05-11.pdf.
[31] O. Chubar, P. Elleaume, and J. Chavanne, A three-dimensional magnetostatics computer code for insertion devices, J. Synchrotron Radiat. **5**, 481 (1998).
[32] H. A. Bethe, Molière's theory of multiple scattering, Phys. Rev. **89**, 1256 (1953).
[33] K. A. Olive *et al.* (Particle Data Group Collaboration), Review of particle physics, Chin. Phys. C **38**, 090001 (2014), Sec. 32.3, p. 401.
[34] A. Rose, Television pickup tubes and the problem of vision, Adv. Electron. Electron Phys. **1**, 131 (1948).
[35] A. Minor, S. A. S. Asif, Z. Shan, E. A. Stach, E. Cyrankowski, T. J. Wyrobek, and O. L. Warren, A new view of the onset of plasticity during the nanoindentation of aluminium, Nat. Mater. **5**, 697 (2006).